AIAA-94-0163

On the Vortical-Flow Prediction Capability of an Unstructured-Grid Euler Solver

F. Ghaffari
NASA Langley Research Ceneter
Hampton, VA

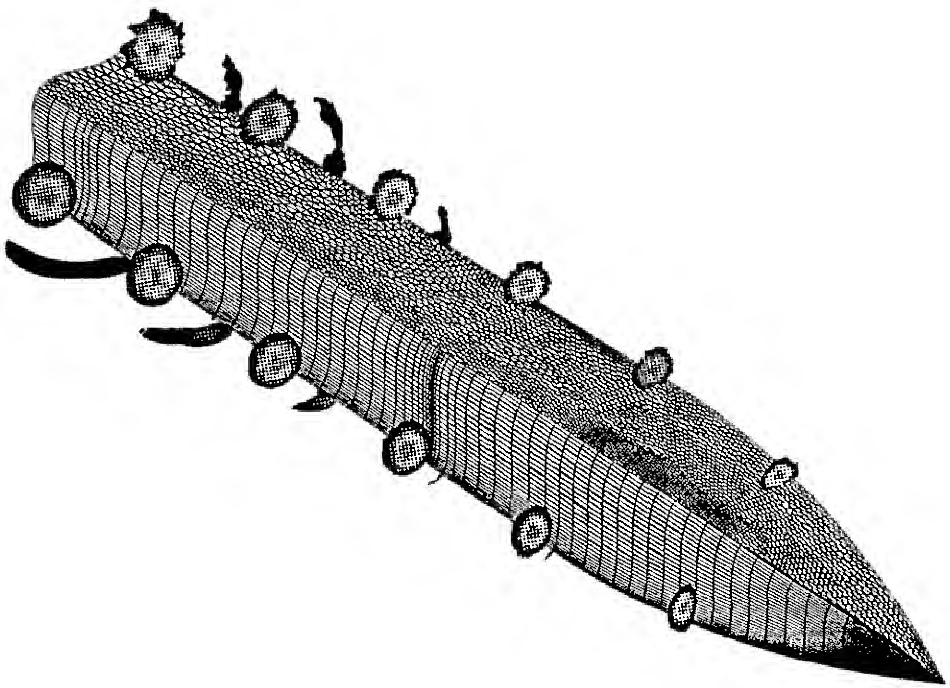

AIAA 32nd Aerospace Sciences Meeting and Exhibit

January 10-13, 1994/Reno, Nevada

On the Vortical-Flow-Prediction Capability of an Unstructured-Grid Euler Solver

Farhad Ghaffari†
Transonic Aerodynamics Branch
Applied Aerodynamics Division
NASA-Langley Research Center, Hampton, Va. 23665

Abstract

The results from a concentrated computational effort are presented with the primary objective being directed at evaluating the vortical-flow-prediction capability of an unstructured-grid Euler solver. Both viscous and inviscid solutions, obtained from an established structured-grid method, along with an experimental wind-tunnel data are used as bench-mark measures to assess the validity of the unstructured-grid Euler results. Viscous effects on vortical flows are first identified by comparing the viscous and inviscid solutions obtained from the structured-grid method. Computational data analysis are then presented which reveal excellent correlations between the inviscid structured and unstructured-grid results in terms of off-surface flow structures, surface pressure distribution and the predicted longitudinal aerodynamic characteristics. The sensitivity of the unstructured-grid inviscid solutions to grid refinement is also discussed along with an analysis of the convergence and performance characteristics for each method.

Nomenclature

C_D	drag coefficient, Drag/$q_\infty S_{ref}$
C_{Do}	measured drag coefficient at $C_L = 0$
C_L	lift coefficient, Lift/$q_\infty S_{ref}$
C_m	pitching moment coefficient, pitching moment/$q_\infty S_{ref} c_{ref}$, moment reference center at $1.86c_{ref}$
C_p	pressure coefficient, $(p - p_\infty)/q_\infty$
c_{ref}	reference chord, 10.92 inches
FS	fuselage station
M_∞	freestream Mach number
$MTVI$	modular transonic vortex interaction
p	static pressure
p_o	free-stream total pressure
$p_{o,l}$	local total pressure
$p_{o,l}/p_o$	normalized total pressure
p_∞	freestream static pressure
q_∞	freestream dynamic pressure
R_{ft}	Reynolds number per foot
S_{ref}	area of reference wing planform, 104.1 in^2
v^*	wall-friction velocity, $\sqrt{\tau_w/\rho}$
X	longitudinal fuselage station, inches
y^+	inner-law variable, yv^*/ν
α	angle of attack, degrees
μ	viscosity
ν	kinematic viscosity, μ/ρ
ρ	density
τ_w	wall shear stress

Introduction

The unstructured-grid approach is an emerging new technology with a tremendous potential to ease the application of Computational Fluid Dynamics (CFD) methodologies for solving the flow about complex configurations in a timely manner. Unlike the conventional structured-grid approach which uses hexahedral elements to discretize a computational domain about a given aerospace vehicle, this new technology utilizes unstructured tetrahedral meshes. The inherent flexibility with which a tetrahedral mesh can conform to a geometrically complex configuration is generally considered to be the primary advantage of the unstructured-grid approach over the structured-grid method. However, as the initial development of the technology is maturing, other advantages have been identified such as solution-adaptive grids. Progress has been made in the past few years in both the tetrahedral-mesh generation techniques (Refs. 1-4) as well as solution algorithms (Refs. 5-9). However, unstructured-grid methodology still has some fundamental shortcomings which hinder its full potential applicability to complex configuration across a wide range of flow conditions.

One of the major impediments to a wide spread application of this new technology is presently due to its restricted viscous-flow capability. Some progress has been made in computing the viscous flow about 2-D airfoils and with limited success for simple 3-D configurations. These viscous flow calculations are generally performed on so called hybrid grids which incorporate certain structured-mesh arrangements near the surface to facilitate the boundary-layer flow-resolution. An example of such grid is the prismatic/tetrahedral mesh (Refs. 10-11) arrangement where prism cells are generated, in a quasi-structured fashion, from a triangulated surface grid definition. These prisms are generally confined to the viscous layer region beyond which a conventional unstructured grid generation method such as advancing front (Refs. 1, 2) or Delaunay triangulation (Refs.

†Research Engineer, Senior member AIAA

12, 13) can be utilized to fill in the inviscid field without constraints. Another example of a hybrid grid is to simply use a structured grid to resolve the boundary-layer flow and couple that to an inviscid unstructured-grid (Refs. 14, 15). In general, it appears that the obvious challenge for extending the present unstructured grid technology to simulate viscous flow is dependent on the development of an innovative approach for generating highly stretched meshes. It would also be advantageous for any new unstructured-grid generation approach to include directional features to accommodate some of the existing algebraic turbulence models that are presently in use in structured-grid methodologies.

Recently there have been a number of successful inviscid-flow analyses performed about fairly complex configurations using the existing state-of-the-art unstructured-grid technology (Refs. 16, 17). These applications have clearly demonstrated the inherent flexibility associated with tetrahedral meshes to conform, as well as being generated in a timely manner, about complex configurations. These advantages coupled with the inviscid-flow approximation (requires less intense computations, in terms CPU-time, compared to viscous flow simulations) provide an efficient computational method that can be used for the flow analysis of certain aerodynamic problems for which the viscous effects are known to be small, such as vortex-flow separation from a sharp-edged configuration. The latter computational method can also be used in the early configurational design to study the relative aerodynamic performance and trends due to a change in the geometrical components. Although, the inviscid computational-method provides a viable engineering tool for the preliminary flow analysis of a given aerodynamic problem, particular attention should be paid for the interpretation of the final results and their dependencies on the fluid viscosity. As a result, the viscous effects have to be clearly quantified in order to eliminate the element of uncertainty which is always associated with an inviscid-flow analysis, in particular when correlated with experimental data.

The objective of the present investigation is to address the validity of the inviscid results obtained, from an algorithm that utilizes tetrahedral-mesh to discretize the computational domain, at conditions that are conducive to flow separation leading to vortical-flow structures. The present study takes advantage of the only possible approach which is to use the computational results from an established structured-grid methodology as a bench mark to assess the validity of the unstructured-grid solutions. The present code-calibration strategy is broken into three steps as follows; (1)- Assess the accuracy of the structured-grid results by comparing the turbulent, thin-layer Navier-Stokes solutions with experimental data. (2)- Isolate the effect of viscosity by complementing the above viscous computations with an inviscid analysis within the structured-grid framework. (3)- Assess the validity of the inviscid unstructured-grid results by comparing them to those obtained with inviscid structured-grid. Both the structured- and the unstructured-grid flow-solvers used in the present investigation, known as CFL3D (Refs. 18-21) and USM3D (Ref. 9) respectively, are developed at NASA Langley Research Center.

Configuration of Interest

The configuration used in the present code calibration study is the isolated fuselage component of a wind-tunnel model, referred to as Modular Transonic Vortex Interaction (MTVI) model, shown in figure 1(a). The complete MTVI model employs a 60° sharp-edged cropped-delta wing with segmented leading-edge flap, and a chine shaped fuselage. In addition, the model is built to be fitted with two different vertical tail arrangements; a single centerline tail or an alternative twin outboard tails as shown in the figure. The model has been tested at various flow conditions, to investigate the interactions between the chine-forebody vortices and different vertical tail arrangements, in the 7- by 10-foot High-Speed-Tunnel at NASA Langley Research Center. In addition to the wind-tunnel testing of the full MTVI configuration, several runs were made with the isolated fuselage primarily to support this computational effort. A photograph of the isolated MTVI fuselage wind-tunnel model, mounted on the sting, is shown in figure 1(b). Two typical flow condition, listed in table 1, were selected from the latter test for the present code-calibration study.

α	M_∞	$R_{ft} \times 10^6$
19.8°	0.4	2.4
29.8°	0.4	2.3

Table 1. Selected flow-conditions.

The rational for simplifying the MTVI configuration for the present code calibration study is primarily dictated by the geometrical complexity associated with the complete MTVI configuration and the foreseen difficulties with the structured-grid application part. These difficulties include the development of a multi-block grid-strategy that is suitable to the existing flow solver as well as the actual flowfield grid generation. These difficulties actually prompted the present code-calibration study to assess the vortical-flow-prediction capability of the unstructured-grid methodology so that

it could subsequently be applied to the full MTVI configuration with confidence. The isolated MTVI fuselage geometry incorporates sharp leading-edges on both the chine forebody as well as the exposed wing-fuselage juncture. Such surface discontinuities, introduced by the sharp leading-edges, are the principle cause of flow separation which subsequently leads to the formation of the vortical-flow structure. This type of flow separation is generally known to be insensitive to viscous effects which make it particularly appropriate for the present inviscid code-calibration study of vortical flows.

Experiment

The wind-tunnel experiment is conducted in the NASA Langley 7- by 10-foot High Speed Tunnel (Refs. 22, 23). This is a closed circuit, continuous-flow atmospheric tunnel with a solid wall test section 6.6 feet high, 9.6 feet wide, and 10 feet long. The tunnel operational Mach number range from 0.0 to 0.9 with maximum Reynolds number of about 4 million per foot.

The MTVI wind-tunnel model is instrumented to measure surface static pressures at three longitudinal stations on the forebody and three longitudinal stations on the aft fuselage that are extended outboard onto the wing surface. The pressures are measured on both sides (i.e., starboard and port) of the model designed to address the flow asymmetry, if any. These pressure stations are highlighted in Fig. 1(a). The sting-mounted wind-tunnel model was equipped with an internally mounted strain gauge balance to measure the six-component forces and moments. The wind-tunnel testing of the isolated MTVI fuselage (see fig. 1(b)) uses similar mounting apparatus for measuring the forces and moments. However, surface static pressures are measured only at the three longitudinal stations on the forebody. These fuselage stations (FS) are located at X=6.1, 10.45, and 14.5 inches measured from the nose apex. For reference, the total fuselage body length is 32.48 inches.

The measured wind-tunnel data are corrected for effects associated with angle-of-attack, wall interference and the model base pressure. The model support system incorporated a pitch sensing device to measure the angle-of-attack which is subsequently corrected to account for the balance and sting deflection under load. The wall interference effects are accounted for through the notions of blockage (ref. 24) and jet boundary (ref. 25) correction principles. The model-base pressures are measured for correcting the data to exclude the resulting force acting on the base of the model. The latter correction is employed to re-adjust the base pressure to that of the freestream static pressure.

Computational Methods

This section provides a brief background on the computational methods used in the present investigation along with some of their respective capabilities.

CFL3D: The unsteady Reynolds-averaged Navier Stokes equations are solved in a body-fitted coordinate system. The algorithm is based on cell centered, finite volume approach incorporating upwind-biased, flux-difference splitting for the inviscid terms. Several turbulence modeling capabilities are implemented, however, the present computational effort only uses the Baldwin & Lomax model (Ref. 26) with Degani & Schiff (Ref. 27) modification to account for massive crossflow separation. The code capabilities and some of the new improvements made over the past few years are evaluated and discussed in references 18-21. For applications to complex configuration, the method has been recently extended to multiblock structured grids with the concept of generalized surface patching (Ref. 21) which has been successfully applied to the F/A-18 aircraft configuration (Ref. 28).

USM3D: The time dependent, three dimensional Euler equations are solved in a computational domain discretized by tetrahedral-mesh elements. Similar to CFL3D, USM3D is based on cell centered, finite volume approach which also uses an upwind flux-difference splitting method. An implicit Gauss-Siedel scheme has recently been implemented to advance the solution (Ref. 29). Convergence to steady state is accelerated with a local time stepping. Further details are discussed in reference 9 and the results from some recent applications can be found in references 16 and 17.

Computational Grid Attributes

Surface Definition: The isolated MTVI fuselage configuration is 32.48 inches long, 4.80 inches wide and 3.00 inches thick. An oblique view of one-half the configuration surface definition used in both viscous and inviscid structured-grid analysis is shown in figure 2. The complete geometry is defined analytically with the exception of a small area, referred to as the "blended region" shown with dotted lines in the figure, which will be discussed later. The forebody portion is 15.08 inches long and defined in two parts with a longitudinal dividing cross-section at X=10.45 inches, where X is measured from the nose apex. The planform and the profile for the front part of the forebody is defined analytically by a circular-arc while the corresponding cross-sectional geometry is defined by a cubic relationship. The geometry for the back part of the forebody is defined by longitudinally repeating the base cross-section of the front part up to where the wing leading-edge intersects the fuselage (i.e., X=15.08). The forebody cross-sectional definitions are spaced longitudinally so that there are three stations that match those of wind-tunnel model

pressure stations. These fuselage stations are denoted in fig. 2.

The fuselage geometry aft of the forebody is generated by modifying the chine leading-edge definitions to incorporate the streamwise thickness associated with the wing-fuselage juncture. The forward part of the wing-fuselage juncture is defined by a circular-arc up to where the wing maximum thickness occurs (X=21.08), beyond which it remains constant. The fuselage geometry aft of the forebody was then completed by adding the surface definition for the blended region. That information was extracted from the Computer Aided Design (CAD) surface patch definition used to build the wind-tunnel model. This blended region describes the area where the leading-edge thickness, (i.e., added to the chine sharp-leading-edges to accommodate for the wing thickness) is smoothly blended inboard with the analytically defined cross-sections.

The computational surface grid definition for the isolated MTVI fuselage is defined with two networks; the first includes the forebody geometry whereas the second consists of the aft fuselage. Each network has 35 longitudinal stations. There are 61 and 69 circumferential grid points per station in the first and second network, respectively. A total of 4,550 grid points are used to define the computational surface geometry. The grids are clustered, with a cosine-like spacing, near all the sharp leading-edges, plane of symmetry and the network boundaries. Furthermore, to ensure smooth outflow conditions at the base, a third network was added which is nominally a body-length downstream extension of the configuration base cross-section defined with 18 longitudinal stations.

Structured Flowfield-Grid: The body slenderness associated with the MTVI fuselage geometry is primarily used to guide the flowfield grid-strategy and topology selection. This led to the selection of a longitudinally-patched multiblock grid-strategy, with a C-O topology for the forebody block, an H-O for the aft fuselage and the downstream grid extension. The flowfield grid is generated with an in-house developed code that is based on transfinite interpolation techniques and have been successfully applied to various configurations in the past (Refs. 30, 31). A turbulent flowfield grid is first generated with sufficient normal clustering near the surface to adequately resolve the laminar sublayer associated with the turbulent boundary layer flow at the subject freestream conditions ($\alpha = 19.8°$, $M_\infty = 0.4$, $R_{ft} = 2.4 \times 10^6$). This grid produced an average normal cell size next to the wall of approximately 0.0005 inches (i.e., $1.5 \times 10^{-5} l$, where l is the total configuration body length) which corresponds to $y^+ \approx 3$. The farfield boundary is located approximately one body length away in the radial direction.

The viscous computations, with turbulent-flow assumptions, are first performed in an effort to determine the approximate thickness of the boundary-layer. A detailed flow analysis of the converged turbulent solutions revealed that the boundary-layer flow is resolved with about 18 cells near the plane of symmetry at a mid-body station. Subsequently, the inviscid flowfield grid is generated by redistributing the points radially within the existing viscous grid blocks. The inviscid nearfield grid is generated by ensuring that an average normal cell size, next to the wall, approximately matched the edge of the turbulent boundary-layer at a mid-body station. At this station, the inviscid normal cell size next to the wall is determined to be about 0.1 inches (i.e., $3.1 \times 10^{-3} l$) which can roughly occupy about 24 viscous cells. Figure 3, shows an isometric farfield (a), nearfield (b) views of both the viscous (dotted lines) and inviscid (solid lines) structured-grids that are superimposed over one another. As evident in Fig. 3(b), the inviscid flowfield grids are generated in such a manner that the nearfield grid density (region where the primary vortex structure is expected to occur) remain roughly the same as those of the viscous grid. The final viscous and inviscid flowfield grids contained 65 and 49 points in the radial direction, respectively. Similarly, there are a total of 376,480 and 283,808 points in the complete viscous and inviscid flowfield grid, respectively.

Unstructured Flowfield-Grid: The strategy used to generate the unstructured grid about the MTVI fuselage configuration is primarily guided by the structured grid analysis. These strategies include the use of the existing structured surface grid definition as the data base for generating the surface triangles. Similarly, the flowfield grid boundaries such as the plane of symmetry, farfield and the outflow are chosen to be identical to those used in the structured grid analysis. The surface and the flowfield grid boundaries are initially triangulated. The desired grid distribution as well as the spacing on both the surface and the flowfield grid boundaries are controlled by a set of parameters determined from coupling a uniform Cartesian background grid with a series of point/line source elements (Ref. 32). The surface triangular elements are generated so that the cell density and spacing, such as around the leading-edges, are comparable to those generated with the structured grids. A similar approach is also adopted to generate the desired grid density and spacing in the flowfield boundaries (i.e., plane of symmetry, farfield, and the outflow plane) comparable to the structured grids. Subsequently, the triangulated surface and the flowfield boundaries are used to generate the corre-

sponding volume tetrahedral-mesh with the advancing front method known as VGRID3D (Ref. 3). Figure 5 presents the final unstructured grids from a similar vantage point as the structured-grid arrangement shown earlier in figure 3.

Despite much attention being paid to minimizing the differences between the unstructured and its counterpart structured grid, in terms of density and spacing, the final grids still contain some dissimilar characteristics. One of the distinct dissimilarities can be attributed to the cell aspect-ratio. Unlike structured grids, the unstructured grid generation techniques, such as the present advancing front, are primarily designed to generate cells having a unit aspect ratio. In the present investigation, this limitation coupled with the constraints in the desired grid density and spacing, was foreseen to lead into an unacceptable number of cells in the final volume grid, which would have about six times more cells than the structured-grid. In an effort to alleviate this discrepancy, the present unstructured grids are generated with an aspect ratio of about three. The effect of this simple grid stretching in the axial direction was significant enough to reduce the total number of cells by a factor of about three. The final unstructured-grid domain consisted of about 102,000 nodes and 567,000 cells which is roughly twice as many cells as used in the inviscid structured-grid. The primary reason for the excess number of tetrahedra is related to the differences in cell aspect-ratio. These differences can clearly be seen by comparing the surface grid stretching in the axial direction in Figs. 4 and 2. The present investigation did not seek to generate a tetrahedral mesh with higher aspect-ratio due to 1)- the anticipated difficulties with grid generation and 2)- the sensitivity of solutions from USM3D to highly stretched tetrahedral meshes has not been fully addressed.

Results and Discussion

The results from the present code calibration study will be discussed in three categories with intention of highlighting the vortical flow prediction capabilities of the present unstructured-grid methodology. These categories include the off-surface flow simulation, surface pressure and the force and moment predictions. In each category the inviscid computational results obtained from the unstructured-grid method will be correlated with complementary solutions acquired with the structured-grid method for both the inviscid as well as the thin-layer Navier-Stokes with turbulent flow assumptions.

Off-surface flow correlations: A composite image summarizing the computational results in terms of normalized total-pressure contours $(p_{o,l}/p_o)$, obtained at $\alpha = 19.8°$, $M_\infty = 0.4$, $R_{ft} = 2.4 \times 10^6$ from both the structured and unstructured-grid methodologies, are presented in figure 6 for various cross-flow planes. The figure has been constructed such that the vertical plane of symmetry, relative to the isometric view of the surface grid representation as shown in the figure, divides the computational results into two parts; the structured-grid solution part (i.e., starboard) and the unstructured-grid solution part (i.e., port side). Coupled with the surface grid representations are the corresponding inviscid solutions (i.e., gray-scaled normalized total-pressures) shown in six cross-flow planes along the length of the isolated MTVI fuselage. For a more quantitative comparison, the figure also shows the predicted normalized total-pressure contours as well as the corresponding cross-sectional geometries, from a head-on vantage point, for the first three stations on the forebody. To assess the viscous effects on the resulting vortex-flow structures, the turbulent-flow solutions computed by the structured-grid method are also included for the same three cross-sectional geometries. It should be noted that these three forebody stations are chosen to be identical to those experimentally measured pressure stations and also the normalized total-pressure contours are plotted over the same range $((p_{o,l}/p_o)_{min} = 0.86, (p_{o,l}/p_o)_{max} = 1.0)$ and levels $((p_{o,l}/p_o)_{inc} = 0.0175)$.

The normalized total-pressure contours obtained from the structured-grid viscous solutions indicate a flow structure that can generally be characterized by three features. These flow features include the primary and secondary vortex flow structures as well as a thin boundary-layer region near the surface. The flow separation from the sharp leading edges of the chine configuration is the principal cause for the formation of the primary vortex flow. The core (here defined as the minimum normalized total-pressure) of the primary vortex appears to move up and slightly outboard with increasing axial distance. Also, note that the normalized total-pressure levels in the primary vortex core remain essentially the same with the exception of a slight increase at FS 3. As expected, the normalized total-pressure contours obtained from the structured-grid inviscid solutions reveal only the primary vortex flow structure (see figure 6). Relative to the viscous solutions, the predicted inviscid primary vortex appears to have a similar axial core-trajectory, but with a contour-level structure that is more compact and clustered.

The corresponding normalized total-pressure contours obtained from the unstructured-grid inviscid solutions are shown in the right hand-side column of figure 6 for the same three forebody cross-sectional geometries. As evident, the unstructured-grid inviscid predictions of the primary vortex-flow structure are incredibly close to those computed with the structured-grid

inviscid method in terms of axial core-trajectory and the total-pressure contour levels. This excellent correlation between the structured- and unstructured-grid inviscid solutions for predicting the primary vortex-flow also persists for the aft-fuselage stations. For the latter stations, the corresponding solutions (i.e., gray-scaled normalized total-pressures), in cross-flow planes, are augmented with the isometric view of the surface-grid representations in figure 6.

Surface pressure correlations: The computed spanwise surface pressure coefficients obtained from structured grid methodologies, based on both turbulent and inviscid flow simulations, along with the unstructured-grid inviscid results are presented in figure 7 for the same three stations on the forebody as those used in the previous discussions. In addition, the figure presents the corresponding experimental data measured on both the starboard and port side of the model. Subsequent analysis of the data presented in figure 7 addresses: 1)- the accuracy of the structured-grid viscous solutions in predicting the experimental data; 2)- the viscous effects from the structured-grid solutions; and 3)- the validity of the unstructured-grid inviscid solutions.

The surface pressure coefficients obtained from the structured-grid viscous solutions, with turbulent-flow assumptions, correlate reasonably well with the experimental data for both the upper and lower surface. The agreement appears to be particularly good at FS 2 and FS 3 in the suction-peak region associated with the primary vortex flow. There is also a good surface pressure correlation, at FS 3, in the region where the secondary vortex-flow occurs (located just inboard of the leading edge, see figure 6). However, this agreement is not quite as good at FS 2. The largest surface pressure disagreements between the computational results and data appear to occur at FS 1, where the primary vortex suction peak is underpredicted. The source of this disagreement has not yet been identified, but it could be associated with transitional flow in the experiment which is not computationally modeled.

The viscous effects on the surface pressure coefficients are clearly evident, figure 7, by correlating the two computational solutions (i.e., solid and dashed lines) obtained from the structured-grid method. The correlations indicate that the inviscid solutions develop a primary vortex suction peak that is higher (more negative) and located slightly outboard compared to the viscous results. Unlike the viscous solutions, the computed inviscid surface pressure distribution do not indicate the presence of an inflection point that leads to a region of mild expansion which is directly attributed to the secondary vortex-flow effects. Similar trend has been demonstrated to occur, due to the absence of viscous effects, on a flat delta wing (Ref. 33).

Finally, the inviscid results presented in figure 7 also reveal the correlations between the surface pressure distributions obtained from structured (dash lines) and unstructured-grid (dash-dot lines) methodologies. The correlations clearly indicate an excellent agreement between the results both in terms of magnitudes as well as the overall characteristics at all stations examined.

Similar procedures were employed to compute the flow about the isolated MTVI fuselage at a higher angle of attack. The computational results based on both structured- and unstructured-grids are obtained at $\alpha = 29.8^\circ$, $M_\infty = 0.4$, $R_{ft} = 2.3 \times 10^6$ with available experimental data. The computed surface pressure distributions obtained from these solutions are presented in figure 8 along with the corresponding experimental data. Very similar conclusions can generally be drawn from these results as those identified previously for the flow conditions at $\alpha = 19.8^\circ$, $M_\infty = 0.4$, $R_{ft} = 2.4\times10^6$. In particular, note the excellent correlations between the structured- and unstructured-grid inviscid solutions.

Forces and moment correlations: The predicted longitudinal aerodynamic characteristics are correlated with those measured experimentally over the isolated MTVI fuselage model in figure 9. The wind-tunnel data is presented over the entire range of flow-conditions tested, while the computational results are obtained for those conditions listed in table 1. Similar to previous figures (7, and 8), the results shown in figure 9 are intended to provide a measure for assessing: 1)- the accuracy of the structured-grid viscous solutions in predicting the experimental data; 2)- the viscous effects from the structured-grid solutions; and 3)- the validity of the unstructured-grid inviscid solutions.

The computed lift and drag coefficients obtained from the structured-grid viscous solutions (filled circles) compares very well with the measured data (open circles), however the pitching moment appears to have been slightly overpredicted. The viscous effects on the total forces and moment can be identified by comparing the structured-grid viscous (filled circles) and inviscid (filled squares) solutions. Despite the significant influence on the computed surface pressure distributions (see figs. 7 and 8), the viscous effects appear to cause only small change in the total lift, drag, and pitching moment coefficient. Finally, the longitudinal aerodynamic characteristics computed by the inviscid unstructured-grid method (open squares) correlates reasonably well and those obtained from the structured-grid (filled squares) method, for the drag and pitching moment coefficient. However, the lift coefficients appear to have been overpredicted by the unstructured-grid method.

Convergence & Performance characteristics

The present computations are all performed on the Cray-YMP, located either at NASA Ames (Numerical Aerodynamic Simulation (NAS)) or at NASA Langley Research Center. The convergence history for both the viscous/inviscid structured- and inviscid unstructured-grid solutions, obtained at $\alpha = 19.8°$, $M_\infty = 0.4$, $R_{ft} = 2.4\times10^6$, are shown in figure 10. The structured-grid viscous solution took about 2,600 cycles to reduce the residuals by 6 orders of magnitude and limit the C_L oscillations to a negligible level. The structured-grid inviscid solution took 1,500 cycles to reduce the residuals by about 8 orders of magnitude and limit the C_L oscillations to a comparable level as those of the viscous solution. The unstructured-grid inviscid solution required only 500 cycles to reduce the residuals by about 4.5 orders of magnitude with a similar reduction in C_L-oscillation characteristics.

The effects of structured grid refinement on both the viscous and inviscid solutions were not investigated due to: 1)- the adopted viscous grid-strategy (designed to adequately resolve the geometrical complexity along with the corresponding flow physics) are comparable to those that have been found suitable (Ref. 27) for resolving such vortical flows emanating from a sharp-edged configuration. 2)- the rational procedure employed for eliminating the grids in the boundary-layer region (determined by analyzing the viscous solutions from previous step), to generate the inviscid grids. However, since the sensitivity of USM3D solutions to grid refinement has not been addressed for vortical flows, an effort is made here to evaluate that effect for the present unstructured-grid analysis.

Two new unstructured-grids are generated about the isolated MTVI fuselage; one coarser and the other finer with respect to the baseline grid. The coarse grid employed cell sizes that are globally about 15% larger while the fine grid used cell sizes that are about 10% smaller, compared to the baseline grid. Similar procedures are employed to obtained the solutions for the coarse and fine grids as those used with the baseline grid. The spanwise surface pressure distributions computed at $\alpha = 19.8°$, $M_\infty = 0.4$, are shown in figure 11 for the same three fuselage stations used in previous correlations. The corresponding number of surface triangles as well as the total number of cells for each grid strategy are also denoted in the figure. The correlations indicate that the baseline grid provides adequate grid size and density to resolve the subject flow due to the small sensitivity of the corresponding surface pressure coefficients to further grid refinement.

The computational efficiency and performance characteristics of the present unstructured-grid method are contrasted, in figure 12, against those of the structured-grid method obtained from both inviscid and viscous analysis. Particular attention should be paid to account for the disparity in the total number of cells used by each computational method (unstructured-grid has more than twice the number of cells) before interpreting the other statistics presented in the table such as the memory requirement and total CPU time. As discussed earlier, this disparity in the total number of cells is primarily attributed to the constraint (i.e., mild cell stretching in the axial direction) imposed by the present unstructured-grid generation method. Improvements to this constraint, to allow for tetrahedral-mesh generation with a comparable axial stretching as those of the structured-grids, should at least alleviate the existing differences (in terms of memory requirements and CPU-time) by a factor of about two. Despite the latter improvement however, the unstructured-grid technology is generally known to be more computationally intense, both in terms of memory requirements and the computational time, due to the random nature of the grid distribution. Nonetheless, these computational resource requirements can be trade-offs for the quick turn-around time to generate meshes around complex configurations.

Concluding Remarks

Inviscid flow analyses are presented for vortical flow prediction capability of an unstructured grid methodology. The accuracy of the results are verified through a comparison with the computational predictions obtained with the structured-grid technology based on both the thin-layer Navier-Stokes with turbulent assumption as well as the inviscid formulations. The validity of the structured-grid turbulent solutions are first supported by a complementary set of wind-tunnel data. The viscous effects on vortical flow structures are then identified within the structured-grid framework. Subsequently, the structured-grid inviscid results are used to provide the bench-mark measures to evaluate the accuracy of the results obtained from the unstructured-grid methodology. The latter correlations revealed an excellent agreements between the computational results obtained from structured- and unstructured-grid methods in terms of off-surface flow characteristics and surface pressure distributions. The unstructured-grid inviscid solutions with the baseline grid were found to be insensitive to further grid refinement. The convergence history and performance characteristics obtained from each computational method are also contrasted which identifies their respective strengths and weaknesses in terms of resource requirements.

Acknowledgments

The author wish to thank Neal Frink of NASA Langley Research Center, Shahyar Pirzadeh, and Brent Bates of ViGYAN Inc. for their support of unstructured grid calculations, and also Robert M. Hall of NASA Langley Research Center for providing the unpublished experimental data on the isolated MTVI fuselage configuration.

References

[1] Peraire, J., Morgan, K., and Peiro, J., "Unstructured Mesh generation by the Advancing Front Method," von Karman Institute for Fluid Dynamics Lecture Series, Numerical Grid Generation, von Karman Institute, Brussels, Belgium, June 11-15, 1990, pp. 37-66.

[2] Lohner, R., and Parikh, P., "Generation of Three-Dimensional Unstructured Grids by the Advancing Front Method," International Journal of Numerical Methods in Fluids, Vol. 8, No. 10, 1988, pp. 1135-1149.

[3] Parikh, P., Pirzadeh, S., and Lohner, R., "A Package for 3-D Unstructured Grid Generation, Finite-Element Flow Solution and Flow Field Visualization," NASA CR-182090, Sept. 1990.

[4] Peraire, J., Morgan, K., and Peiro, J., "Unstructured Finite Element Mesh Generation and Adaptive Procedures for CFD," AGARD Conference Proceedings, No. 464, AGARD, France, 1990, pp. 18.1-18.2.

[5] Batina, J. T., "Unsteady Euler Algorithm with Unstructured Dynamic Mesh for Complex-Aircraft Aeroelastic Analysis," AIAA Paper No. 89-1189, April 1989.

[6] Barth, T. J., and Jaspersen, D. C., "The Design and Application of Upwind Schemes on Unstructured Meshes," AIAA Paper No. 89-0366, Jan. 1989.

[7] Venkatakrishnan, V., and Barth, T. J., "Application of Direct Solvers to Unstructured Meshes for the Euler and Navier-Stokes Equations Using Upwind Schemes," AIAA Paper No. 89-0364, Jan. 1989.

[8] Mavriplis, D., "Multigrid Solution of the Two-Dimensional Euler Equations on Unstructured Triangular Meshes," AIAA Journal, Vol. 26, No. 7, 1988, pp. 824-831.

[9] Frink, N. T., "Upwind Scheme for Solving the Euler Equations on Unstructured Tetrahedral Meshes," AIAA Journal, Vol. 30, No. 1, 1992, pp. 70-77.

[10] Nakahashi, K., "External Viscous Flow Computations Using Prismatic Grid," Lecture Notes in Physics 414, Napolitano, M., and Sabetta, F. (Eds.), Thirteenth International Conference on Numerical Methods in Fluid Dynamics, Proceedings, Rome, Italy 1992, pp. 280-284.

[11] Ward, S., Kallinderis, Y., "Hybrid Prismatic Tetrahedral Grid Generation for Complex 3-D Geometries," AIAA Paper No. 93-0669, Jan. 1993.

[12] Bowyer, A.; "Computing Dirichlet Tesselations," *The Computing Journal*, Vol. 24, No. 2, 1981, pp. 162-166.

[13] Baker, T. J.; "Three Dimensional Mesh Generation by Triangulation of Arbitrary Point sets," AIAA Paper No. 87-1124, 1987.

[14] Holmes, D. G., Connell S. D., "Solution of the 2D Navier-Stokes Equations on Unstructured Adaptive Grids," AIAA Paper No. 89-1932-CP, pp. 25-39, June 1989.

[15] Nakahashi, K., Obayashi, S., "FDM-FEM Zonal Approach for Viscous Flow Computations Over Multiple-Bodies," AIAA Paper No. 87-0604, Jan. 1987.

[16] Frink, N. T., Parikh, P., and Pirzadeh, S., "A Fast Upwind Solver for the Euler Equations on Three-Dimensional Unstructured Meshes," AIAA Paper No. 91-0102.

[17] Parikh, P., Pirzadeh, S., and Frink, N. T., "Unstructured Grid Solutions to a Wing/Pylon/Store Configuration Using VGRID3D/USM3D," AIAA Paper No. 92-4572.

[18] Thomas, J. L.; Taylor, S. L.; and Anderson, W. K.; "Navier-Stokes Computations of Vortical Flows Over Low Aspect Ratio Wings," AIAA Paper No. 87-0207, 1987.

[19] Thomas, J. L., Walters, R. W., Reu, T., Ghaffari, F, Weston, R. P., Luckring, J. M., "Application of a Patched Grid Algorithm to the F/A-18 Forebody Leading Edge Extension Configuration," *Journal of Aircraft*, Vol. 27, Number 9, P749-756, Sept. 1990.

[20] Vatsa, V. N.; Thomas, J. L., and Wedan, B. W.; " Navier-Stokes Computations of Prolate Spheroids at Angle of Attack," AIAA Paper No. 87-2627-CP, 1987.

[21] Biedron, R. T., and Thomas, J. L., "A Generalized Patched-Grid Algorithm With Application to the F-18 Forebody With Actuated Control Strake," *Computing Systems in Engineering*, Vol. 1, Nos 2-4, pp. 563-576, 1990.

[22] Fox, C. H. Jr.; and Huffman J. K.; "Calibration and Test Capabilities of the Langely 7- by 10-Foot High Speed Tunnel," NASA TMX-74027, 1977.

[23] Fox, C. H. Jr.; "Real Time Data Reduction Capabilities at the Langley 7- by 10-Foot High Speed Tunnel," NASA TM-78801, 1980.

[24] Herriot, J. G.; "Blockage Corrections for Three-Dimensional-Flow Closed-Throat Wind-Tunnels, With Consideration of the Effect of Compressibility," NACA Report 995, 1950.

[25] Gillis, C. L.; Polhamus, E. C.; and Gray, J. L. Jr.; "Charts for Determining Jet-Boundary Corrections for Complete Models in 7- by 10-Foot Closed RectangularWind Tunnels," NACA WR-L-123, 1945.

[26] Baldwin, B. S., and Lomax, H., "Thin Layer Approximation and Algebraic Model for Separated Turbulent Flows," AIAA Paper No. 78-257, 1978.

[27] Degani, D., and Schiff, L. B., "Computation of Supersonic Viscous Flows Around Pointed Bodies at Large Incidence," AIAA Paper No. 83-0034, 1983.

[28] Ghaffari, F., Bates, B. L., Luckring, J. M., Thomas, J. L., and Biedron, R. T., "Navier-Stokes Solutions about the F/A-18

Wing-LEX-Fuselage Configuration With Multi-Block Structured Grids," AIAA Paper No. 91-3291, Sept. 1991.

[29] Frink, N. T., " Recent Progress Toward a Three-Dimensional Unstructured Navier-Stokes Flow Solver," AIAA Paper No. 94-0061, 1994.

[30] Ghaffari, F., Luckring, J. M., Thomas, J. L., and Bates B. L., "Navier-Stokes Solutions about the F/A-18 Forebody-Leading-Edge Extension Configuration," *Journal of Aircraft*, Vol. 27, Number 9, P737-748, Sept. 1990.

[31] Ghaffari, F., Luckring, J. M., Thomas, J. L., and Bates B. L., "Transonic Navier-Stokes Solutions about a Generic Hypersonic Configuration," *Journal of Aircraft*, Vol. 28, Number 6, P381-388, June 1991.

[32] Pirzadeh, S., "Structured Background Grids for Generation of Unstructured Grids by Advancing-Front Method," AIAA Journal, Vol. 31, No. 2, Feb. 1993, pp. 257-265.

[33] Hummel, D., "On the Vortex Formation Over a Slender Delta Wing at Large Angles of Incidence," AGARD-CP-247, Paper No. 15, 1978.

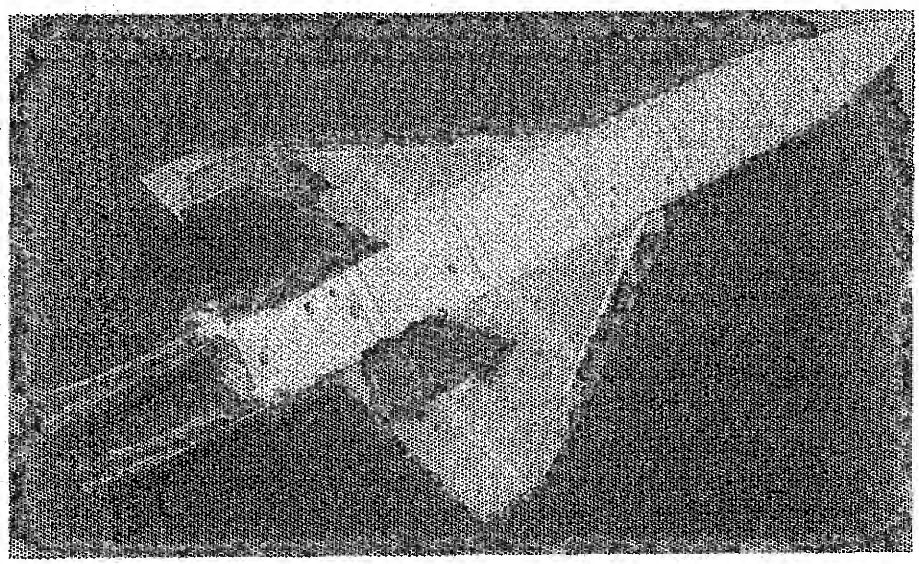

(a) Complete configuration.

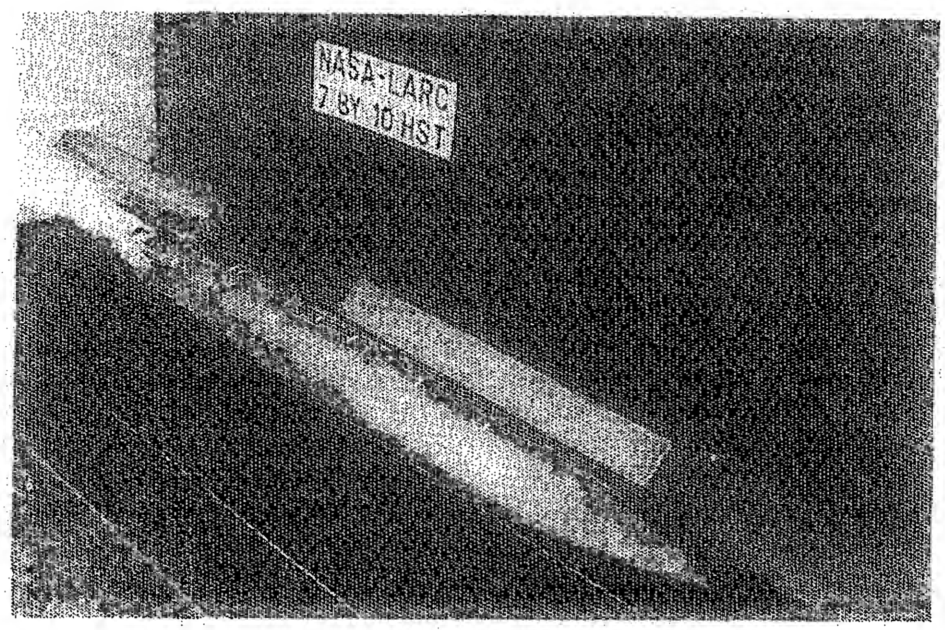

(b) Isolated fuselage.

Fig. 1.- MTVI wind-tunnel model.

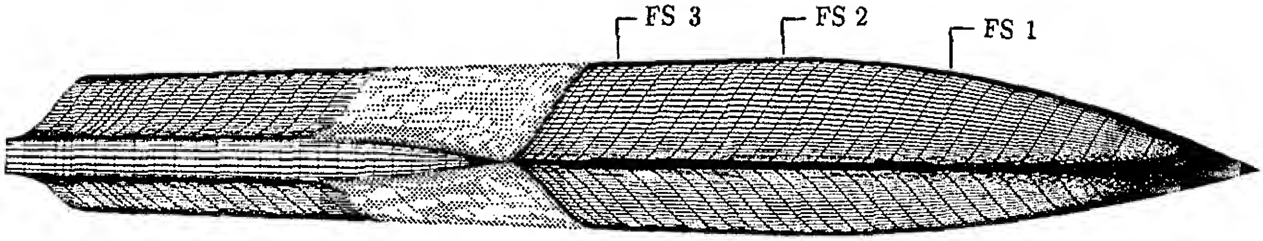

Fig. 2.- Structured surface-grid for the isolated MTVI fuselage .

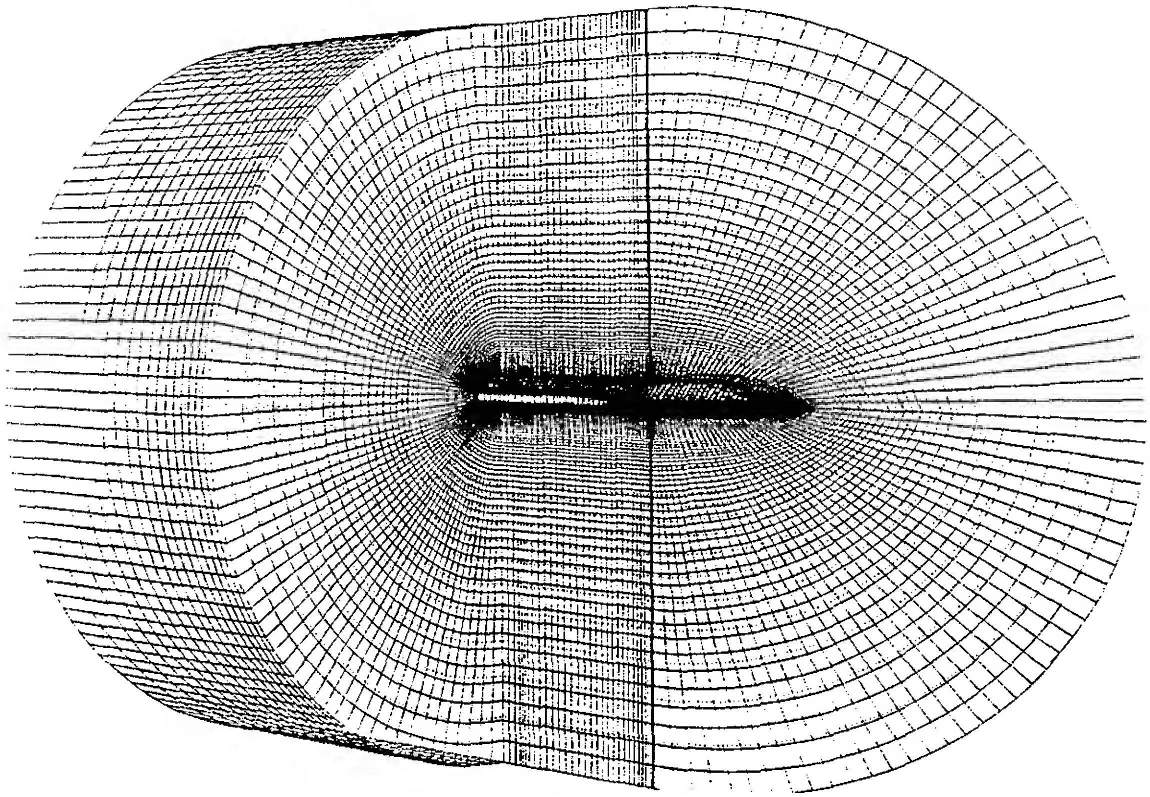

a)- Farfield view

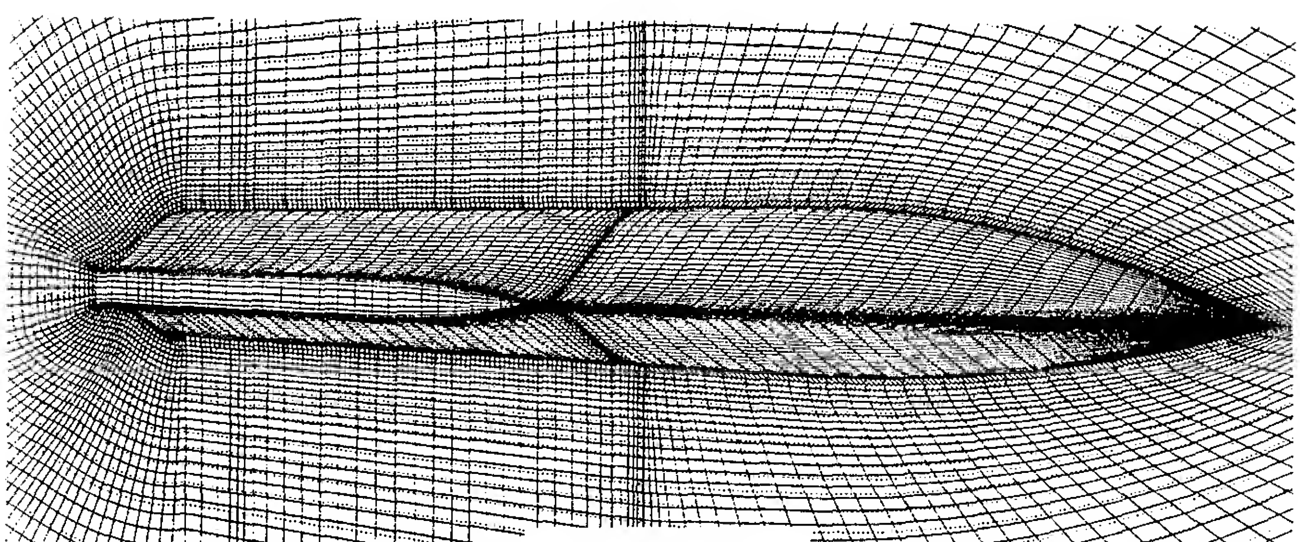

b)- Nearfield view

Fig. 3.- Structured viscous (dotted lines) and inviscid (solid lines) flowfield grid strategies.

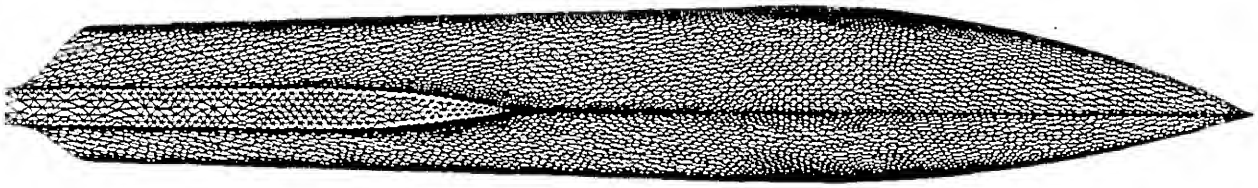

Fig. 4.- Unstructured surface-grid for the isolated MTVI fuselage.

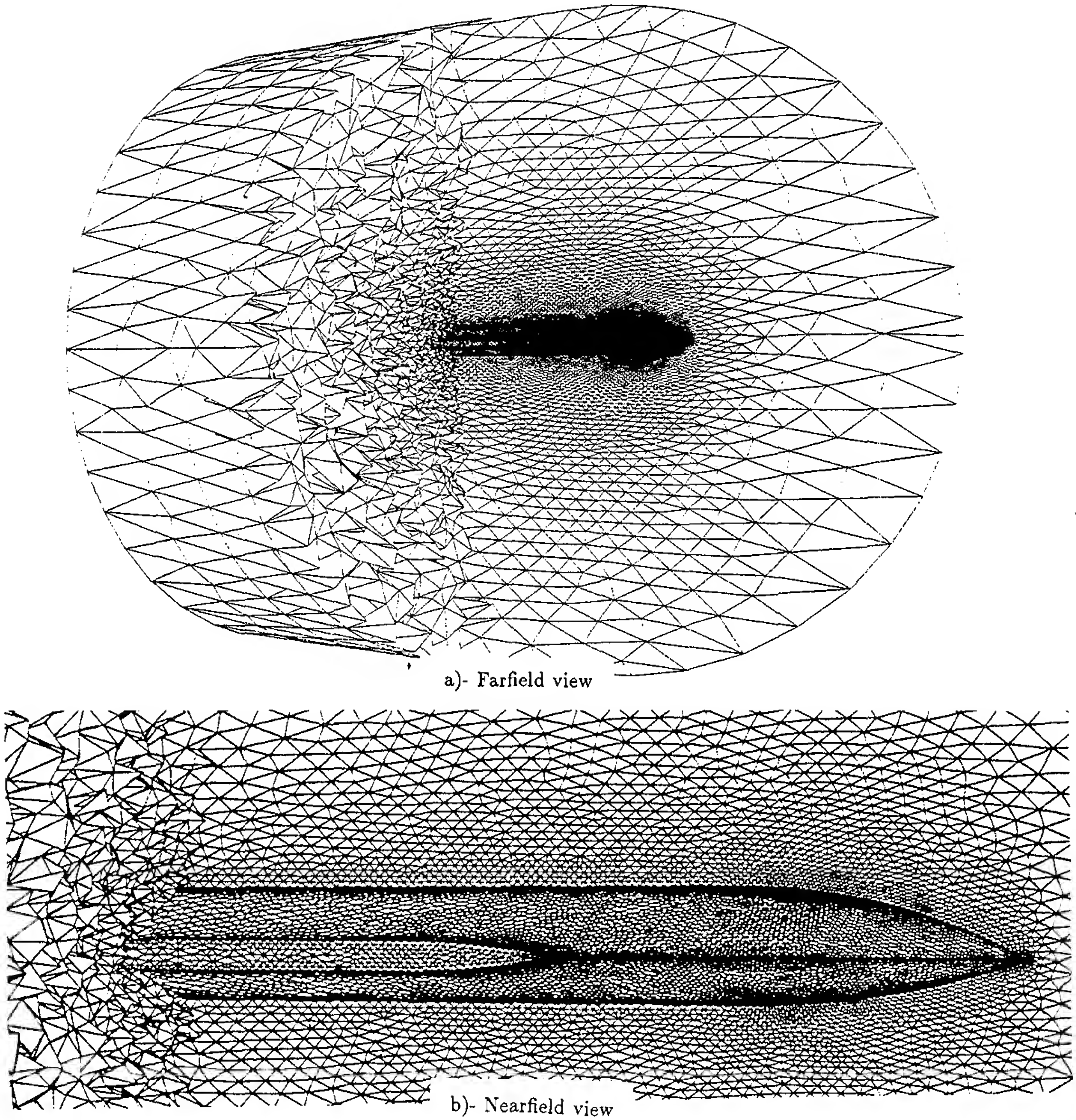

a)- Farfield view

b)- Nearfield view

Fig. 5.- Unstructured inviscid flowfield-grid.

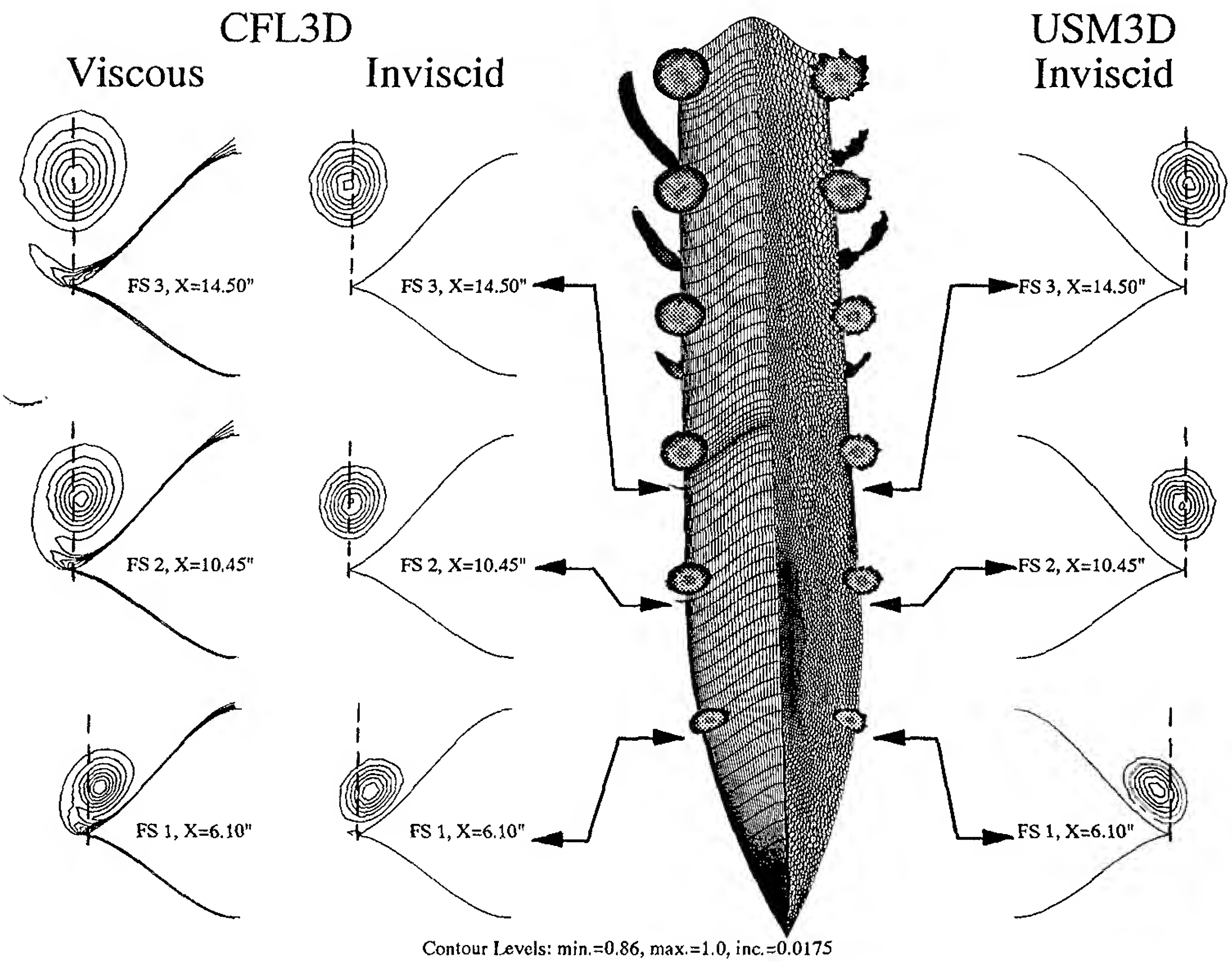

Fig. 6.- Crossflow normalized-total-pressure predictions based on structured and unstructured-grid methodologies; $\alpha = 19.8°$, $M_\infty = 0.4$, $R_{ft} = 2.4 \times 10^6$.

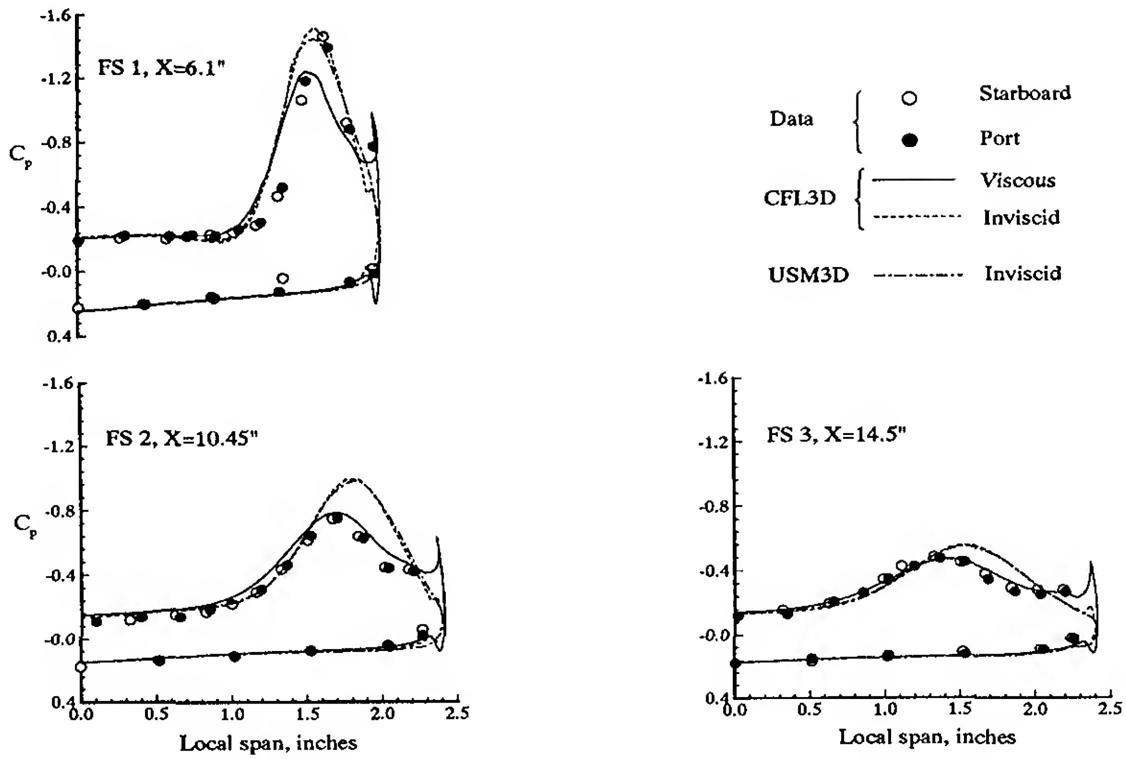

Fig. 7.- Predicted surface pressure coefficients and correlations with data; $\alpha = 19.8°$, $M_\infty = 0.4$, $R_{ft} = 2.4 \times 10^6$.

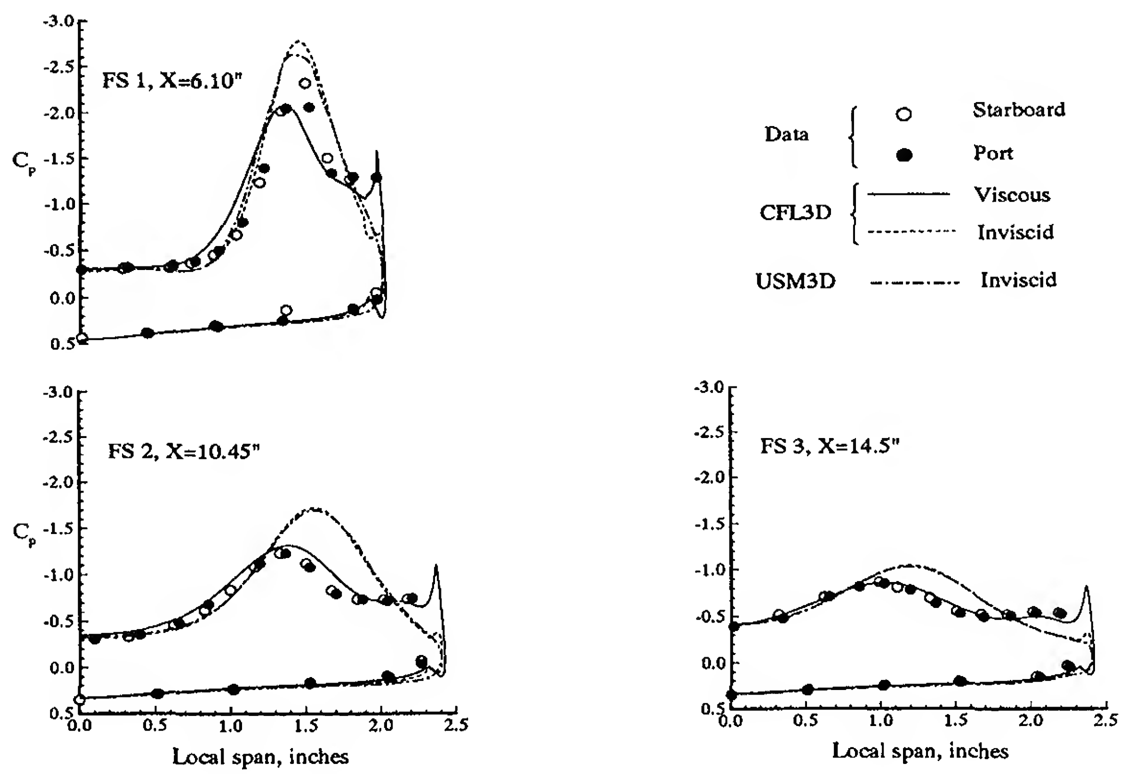

Fig. 8.- Predicted surface pressure coefficients and correlations with data; $\alpha = 29.8°$, $M_\infty = 0.4$, $R_{ft} = 2.3 \times 10^6$.

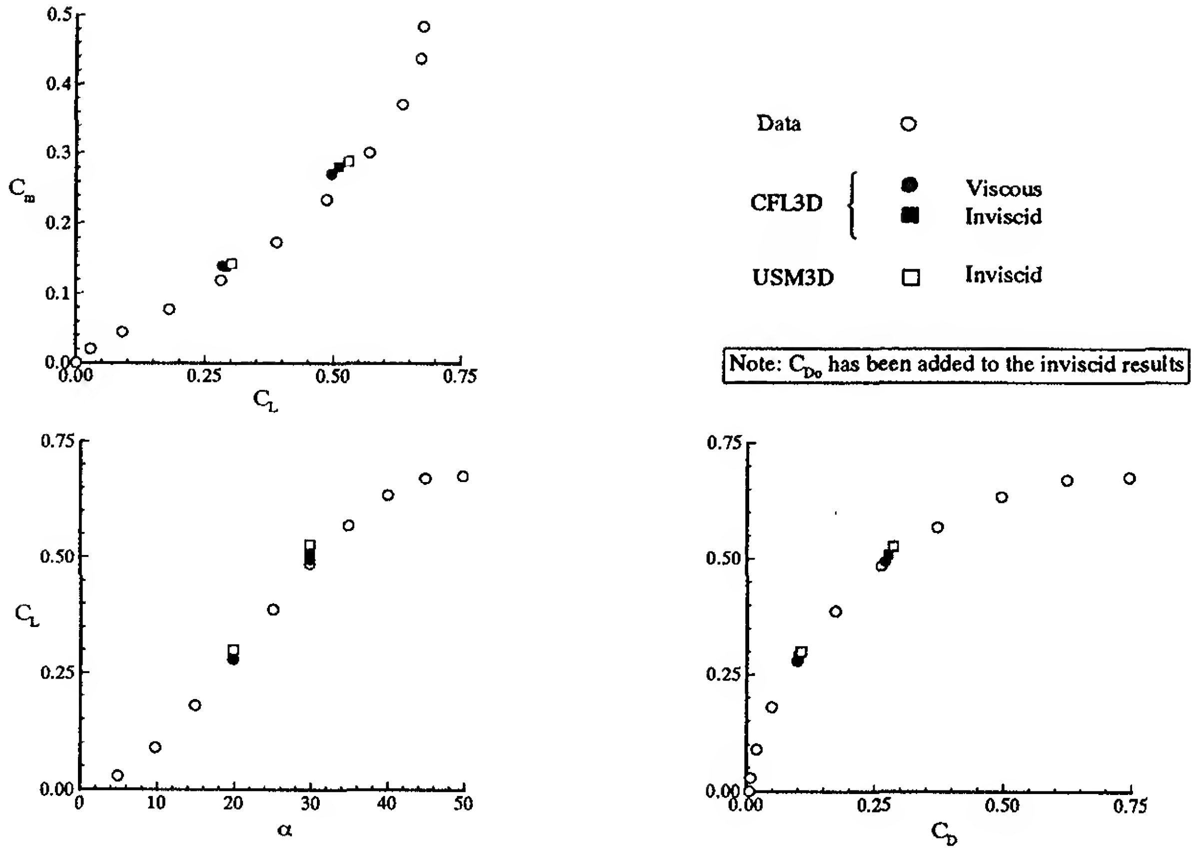

Fig. 9.- Predicted longitudinal aerodynamic characteristics and correlations with data; $M_\infty = 0.4$, $R_{ft} \approx 2 \times 10^6$.

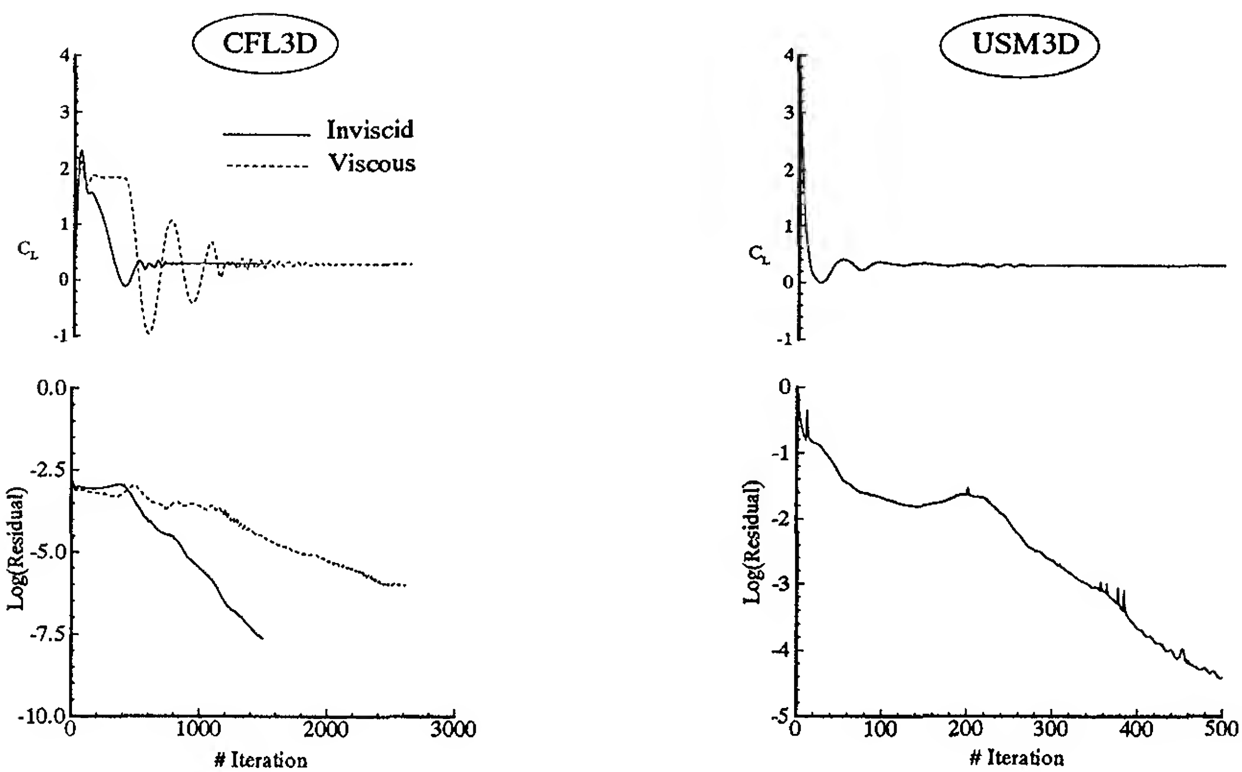

Fig. 10.- Structured/unstructured-grid solutions convergence history; $\alpha = 19.8°$, $M_\infty = 0.4$, $R_{ft} = 2.4 \times 10^6$.

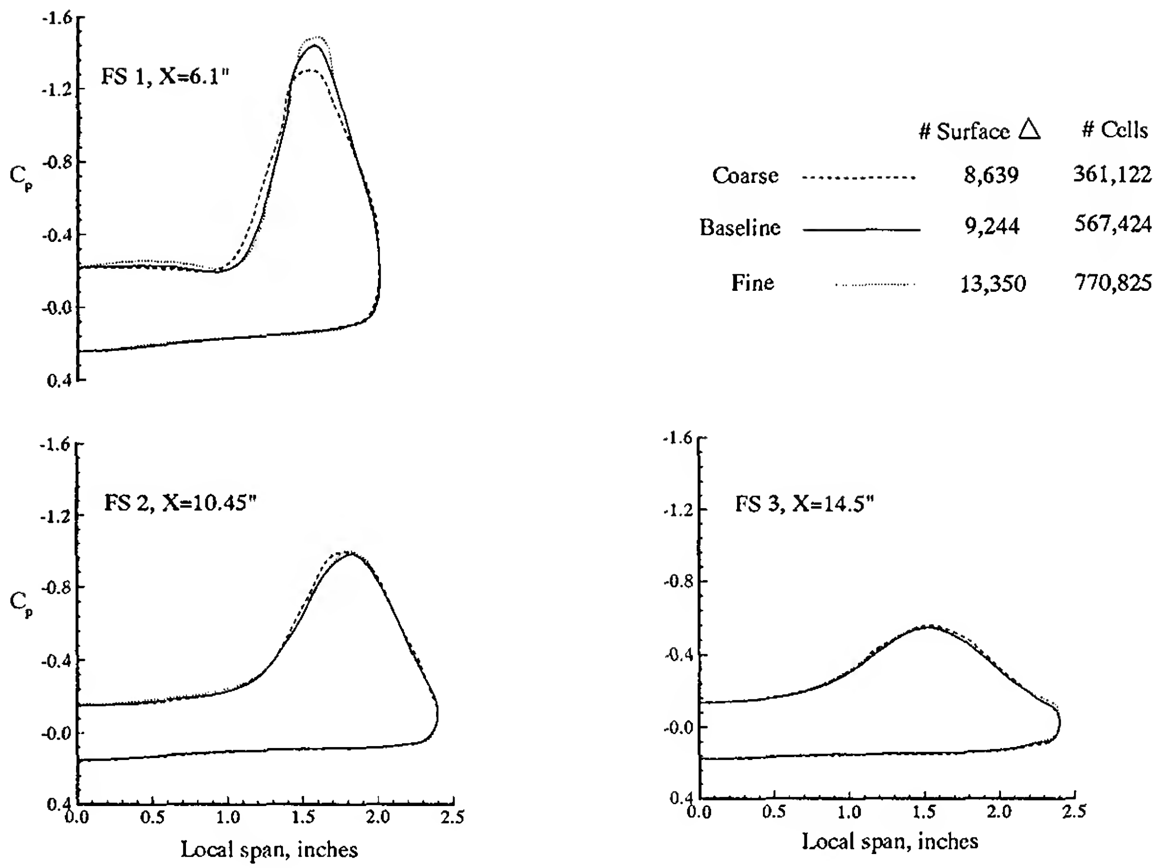

Fig. 11.- Unstructured-grid solution sensitivity to grid refinement; $\alpha = 19.8°$, $M_\infty = 0.4$.

	CFL3D		USM3D
	Viscous	Inviscid	Inviscid
Total # of cells	352,512	264,384	567,424
Total # of surface boundary faces	5,508	5,508	9,224
Memory requirements	15 MW	10 MW	102 MW
Orders of reduction in total residuals	6.1	7.8	4.5
Total # of cycles	2,610	1,500	500
Total CPU time Cray-YMP	3.25 hrs	1.20 hrs	5.1 hrs

Fig. 12.- Structured/unstructured-grid methods performance characteristics; $\alpha = 19.8°$, $M_\infty = 0.4$, $R_{ft} = 2.4 \times 10^6$.